CHEN, L., WANG, S., JIANG, H. and FERNANDEZ, C. 2023. A novel combined estimation method for state of energy and predicted maximum available energy based on fractional-order modeling. *Journal of energy storage* [online], 62, article 106930. Available from: https://doi.org/10.1016/j.est.2023.106930

A novel combined estimation method for state of energy and predicted maximum available energy based on fractional-order modeling.

CHEN, L., WANG, S., JIANG, H. and FERNANDEZ, C.

2023

A novel combined estimation method for state of energy and predicted maximum available energy based on fractional-order modeling

Lei Chen [a], Shunli Wang [a,*], Hong Jiang [a], Carlos Fernandez [b]

[a] *School of Information Engineering, Southwest University of Science and Technology, Mianyang 621010, China*
[b] *School of Pharmacy and Life Sciences, Robert Gordon University, Aberdeen AB10-7GJ, UK*

* Corresponding author.
E-mail address: 497420789@qq.com (S. Wang).

ABSTRACT

Although accurate SOE estimation can enhance the reliability of residual energy prediction, the environmental temperature, parameter coupling, and multiple state constraints increase the difficulty of obtaining SOE accu-rately. A combined estimation method for SOE and predicted maximum available energy based on fractional- order composite equivalent circuit model is proposed to ensure SOE accuracy in the whole battery life cycle. Firstly, the fixed fractional-order forgetting factor recursive least square method is used to realize the online identification of full parameters. Secondly, the adaptive dual fractional-order extended Kalman filter algorithm is applied to realize the co-estimation of SOC and SOE to solve parameter constraints and state coupling. Finally, the fourth-order extended Kalman filter algorithm is exploited to realize the joint estimation of the predicted maximum available energy and SOE, effectively avoiding the divergence of results caused by fixed maximum available energy. The longitudinal comparison experiment results show that the proposed algorithm has the highest accuracy and the smallest root mean square error, which proves the necessity of updating the maximum available energy in real-time. The horizontal comparison experiment further illustrates that real-time correction of multiple factors affecting the SOE estimation accuracy is a necessary way to achieve high accuracy and strong robustness.

Keywords:
Li-ion battery; Fractional-order composite equivalent circuit model; Maximum available energy prediction State of energy; Adaptive double fractional-order extended Kalman filter

1. Introduction

Lithium battery has become one of the best choices for energy storage system (ESS) in many fields due to its high energy density, long cycle life, low self-discharge rate, high safety and reliability, and no memory effect. As an important part of self-powered wireless sensor networks, ESS is the basic guarantee for realizing the optimal utilization of renewable energy in self-powered wireless sensor networks [1]. It can reduce the impact of intermittent and uncertain renewable energy collection on the transmission quality of sensor nodes, improve the utilization rate of renewable energy, significantly reduce the replacement frequency of batteries, and reduce pollution to the natural environment [2].

The battery management system (BMS) of the ESS is mainly used to predict the residual power of the lithium battery. Accurate SOE estimation will effectively reduce the probability of battery damage, fire, and other events, and accurately reflect the battery energy distribution, load balance, energy storage device application safety, and other information, thus extending the working life of the ESS and enhancing its safety [3].

The State of Charge (SOC) cannot reflect the remaining available time, which seriously limits the performance of the battery management system (BMS). The State of Energy (SOE) is defined as the ratio of residual available energy to maximum available energy, and the accurate SOE estimation can enhance the reliability of residual power prediction and further clarify the supply time of residual power, which is very important for the BMS of ESS. Since SOC and SOE cannot be directly measured in practical applications, exploration of novel battery modeling methods and state estimation methods becomes the focus of academia and industry [4,5]. Due to the strong fractional-order characteristics of capacitors, the fractional-order constant-phase components are used to explore the root cause of energy change from the internal reaction mechanism [6–8]. Combined with the characteristics of wide temperature and variable current, the establishment of a battery model with strong adaptability provides new ideas for improving the modeling accuracy of lithium batteries [9].

Factors such as parameter coupling, state constraints, and noise interference during the operation of lithium batteries increase the difficulty of accurately obtaining SOE [10–12]. Therefore, determining the SOE estimation method with high accuracy and strong applicability can not only avoid the adverse effects of environmental factors on the prediction results but also maximize the monitoring role of BMS. The commonly used SOE estimation methods, including the power integra-tion method [13] and open-circuit voltage method [14,15], are simple to calculate, but suffer from large cumulative errors, not suitable for online estimation; Data-driven algorithms [16–18], such as neural networks and support vector machines, are simple in principle but require a large amount of training data; Kalman filter [19,20], particle filter [21], and their derivatives algorithms [22–24] in adaptive filter estimation method have wide practicability and can realize the self-correction function, but each algorithm has certain applicable occasions.

Xu et al [25] proposed a multi-time-scale estimator using dual H∞ filters for SOC and SOE estimation, which proved that the algorithm had certain advantages in practical applications, without considering changes in the maximum available energy. Wang et al [26] proposed a SOC estimation method combining particle filter and fractional-order extended Kalman filter, which had good accuracy and fractional-order real-time performance but had high computational complexity. Shrivastava et al [27] proposed a new adaptive extended Kalman filter based on the double forgetting factor for SOC and SOE joint estimation. Despite considering the identification of model parameters and the quantitative relationship between SOC and SOE, the change of maximum available energy is also ignored. Ma et al [28] studied a data-driven method to estimate SOC and SOE simultaneously and verified the reliability under different temperatures, different battery materials, and noise interference. However, the algorithm required a lot of data and did not consider the variation of the maximum available energy. The above algorithm fully verified the validity and correctness of state estimation combined with fractional-order modeling and filtering method, providing a correct idea for the application of the fractional-order filtering in state estimation.

The maximum available energy will change with the current rate, ambient temperature, and cycle period [29] [30]. Using the fixed maximum available energy to calculate SOE will inevitably reduce the estimation accuracy during the whole battery life and even result in divergence [31,32], which is almost ignored in the existing literatures [33,34]. Given the problems of poor numerical stability and large cross-interference in the existing estimation algorithms, establishing the connection between the maximum available energy and the SOE to improve the accuracy and robustness of the energy state throughout the whole life cycle is the key issue. Therefore, a combined estimation method for SOE and SOC with maximum available energy prediction based on the fractional-order composite equivalent circuit model (FOC-ECM) is proposed, which can real-time correct the maximum available energy and effectively solve the influence of multiple influencing factors such as ambient temperature, parameter coupling, state constraint, and noise interference on the estimation accuracy of SOE in actual operating conditions.

2. Mathematical analysis

2.1. Equivalent modeling

Since characteristics such as open-circuit voltage, capacity, and en-ergy will change with the discharge process, capacity change needs to be considered when establishing the equivalent battery model to improve the adaptability of the model. Due to the fractional-order characteristics of capacitors, the fractional-order composite equivalent circuit model (FOC-ECM) is selected to approximate the dynamic characteristics of lithium batteries, as listed in Fig. 1.

U_{OCV}(SOE, T) is the open-circuit voltage, which is a function of SOE and temperature, defined in Eq. (1). K_0, K_1, K_2, K_3, and K_4 are the undetermined coefficients.

$$U_{OCV}(T,SOE)=K_0(T)-\ K_1(T)SOE(k)-\ K_2(T)/SOE(k)+K_3(T)ln(SOE(k))+K_4(T)ln(1-SOE(k)) \tag{1}$$

The FOC-ECM is composed of a capacity characteristic circuit mod-ule and a FOECM. The left part represents the capacity characteristics. C_Q is defined as a function of the nominal capacity Q_{nom} of the battery, f_1 (*Cycle*) and f_2 (*Temp*) are defined as correction coefficients for battery cycle life and temperature. The mathematical derivation is shown in Eq. (2).

$$C_Q = 3600.Q_{nom}.f_1(Cycle).f_2(Temp) \tag{2}$$

C_1 and C_2 are the element parameters of the capacitance model. The orders of CPE$_1$ and CPE$_2$ elements are expressed as α and β. U_1 represents the partial voltage at the parallel connection of R_1 and CPE1, and U_2 represents the partial voltage at the parallel connection of R_2 and CPE2. According to Kirchhoff's law of voltage and current, the expressions of polarization voltage and the terminal voltage of the circuit can be ob-tained as shown in Eq. (3).

$$\begin{cases} D^{\alpha}U_1 = \dfrac{I}{C_1} - \dfrac{U_1}{R_1C_1} \\ D^{\beta}U_2 = \dfrac{I}{C_2} - \dfrac{U_2}{R_2C_2} \\ U_L = U_{ocv} + U_0 + U_1 + U_2 \end{cases} \tag{3}$$

Eq. (3) is discretized by using the definition of G-L fractional calcu-lus, and the discretized state space equation is simplified as shown in Eq. (4).

$$\begin{cases} \begin{bmatrix} SOE(k) \\ U_1(k) \\ U_2(k) \end{bmatrix} = \begin{bmatrix} 1 & 0 & 0 \\ 0 & -\dfrac{T^{\alpha}}{R_1C_1} & 0 \\ 0 & 0 & -\dfrac{T^{\beta}}{R_2C_2} \end{bmatrix} \begin{bmatrix} SOE(k-1) \\ U_1(k-1) \\ U_2(k-1) \end{bmatrix} + \begin{bmatrix} \dfrac{\eta TU}{E} \\ \dfrac{T^{\alpha}}{C_1} \\ \dfrac{T^{\beta}}{C_2} \end{bmatrix} I_{k-1} - \begin{bmatrix} 0 \\ \sum\limits_{j=1}^{k} \omega_j^{\alpha} U_1(k-j) \\ \sum\limits_{j=1}^{k} \omega_j^{\beta} U_2(k-j) \end{bmatrix} + \omega_{k-1} \\ U_L(k) = U_{OCV}(T,SOE) - [0\ \ 1\ \ 1][\ SOE(k) \quad U_1(k) \quad U_2(k)\ ]^T - R_0I_k + v_{k-1} \end{cases} \tag{4}$$

2.2. Parameter identification

Our previous work [35] has shown that the online identification algorithm is more suitable for model parameter identification under dynamic unknown conditions. Due to the nonlinear relationship between the order of the model and the output variables, the fixed value of the fractional order is obtained by the offline method, and the rest parameters are obtained by the online parameter identification method.

First, according to the full circuit response of the HPPC experiment, the parameters [R_0 R_1 R_2 C_1 C_2] can be calculated. Then, the fractional order α and β are identified. U_1 and U_2 represent the fractional voltage of capacitors C_1 and C_2 respectively, which can be expressed as shown in Eq. (5).

$$\begin{aligned} U_1(t) &= T^{\alpha}\sum_{j=0}^{k}(-1)^j\binom{-\alpha}{j}\left(\frac{I(t)}{C_1} - \frac{U_1(t-jT)}{R_1C_1}\right) \\ U_2(t) &= T^{\beta}\sum_{j=0}^{k}(-1)^j\binom{-\beta}{j}\left(\frac{I(t)}{C_2} - \frac{U_2(t-jT)}{R_2C_2}\right) \end{aligned} \tag{5}$$

The expression of terminal voltage can be further updated as shown in Eq. (6).

$$\begin{aligned} U_L = & U_{ocv} + U_0 + T^{a}\sum_{j=0}^{k}(-1)^{j}\binom{-a}{j}\left(\frac{I(t)}{C_1}-\frac{U_1(t-jT)}{R_1C_1}\right) \\ & + T^{\beta}\sum_{j=0}^{k}(-1)^{j}\binom{-\beta}{j}\left(\frac{I(t)}{C_2}-\frac{U_2(t-jT)}{R_2C_2}\right) \end{aligned} \tag{6}$$

The error between the estimated terminal voltage and the measured terminal voltage of the model is minimized by identifying parameters α and β. The fitness function of the identification parameters is as shown in Eq. (7).

$$finess(\widehat{\theta}) = \min_{\theta}\sum_{k=1}^{N}(|U_L(k) - U_L(I_k, \widehat{\theta})|) \tag{7}$$

where, θ are the parameters α and β to be identified, and N is the data length used for parameter identification.

$U_L(k)$ is the actual terminal voltage and $U_L(I_k, \hat{\theta})$ is the terminal voltage estimated by the fractional order modeling. The fractional orders of a specific SOE pulse can be identified through the particle swarm optimization algorithm. The rest parameters are obtained by the online parameter identification method. The derivation process is shown in Table 1.

3. A novel combined estimation method for SOE and predicted maximum available energy

3.1. A combined estimation method for SOC and SOE

The discretization definition equation of SOC is shown in Eq. (8).

$$SOC(k+1) = SOC(k) + \frac{\eta_{CD}(I)I(k)\Delta T}{\eta_C(I)Q} \tag{8}$$

where η_{CD} is defined as capacity charge-discharge efficiency, a fitting function of current; Q is the rated capacity. SOE is defined by the power integration method, and the discretization equation is shown in Eq. (9).

$$SOE(k+1) = SOE(k) + \frac{\eta_{ED}(I)I(k)U(k)\Delta T}{\eta_e(I)E} \tag{9}$$

where $SOE(k)$ is the energy at time k; η_{ED} is defined as energy charge- discharge efficiency, which is a fitting function of current; E is the maximum available energy. The relationship expression between SOC and SOE is established as shown in Eq. (10).

$$U(k) = \frac{(SOE(k+1) - SOE(k))\cdot\eta_E(I)\cdot E\cdot\eta_{CD}(I)}{(SOC(k+1) - SOC(k))\cdot\eta_C(I)\cdot Q\cdot\eta_{ED}(I)} \tag{10}$$

Combined with the definition of SOE, the discrete state space equation is established as shown in Eq. (11).

$$\begin{cases} SOE(k+1) = SOE(k) + \dfrac{\eta_{ED}(I)I(k)U(k)\Delta T}{\eta_e(I)E} \\ U(k) = \dfrac{(SOE(k+1) - SOE(k))\cdot\eta_E(I)\cdot E\cdot\eta_{CD}(I)}{(SOC(k+1) - SOC(k))\cdot\eta_C(I)\cdot Q\cdot\eta_{ED}(I)} \end{cases} \tag{11}$$

The adaptive dual fractional-order extended Kalman filter algorithm (ADFOEKF) is used to realize the co-estimation of SOC and SOE to improve the estimation accuracy. One Kalman filter is used to estimate SOC, and the other Kalman filter is used to estimate SOE based on SOC estimation results. The AFOEKF has been discussed in our previous work [36], the steps are shown as follows.

(1) Initialization:

$$\begin{cases} \widehat{x}^{+}_{x,0} = E(x_{x,0}) \\ P^{+}_{x,0} = E\left[\left(x_{x,0} - \widehat{x}^{+}_{x,0}\right)\left(x_{x,0} - \widehat{x}^{+}_{x,0}\right)^{T}\right] \end{cases} \tag{12}$$

(2) Time domain update of the state:

$$\widehat{x}_{x,k+1}^{-} = f\left(\widehat{x}_{x,k}^{+}, u_k\right) = A_x x_{x,k} + B_x u_k - \sum_{j=1}^{k} K_{x,j} x_{x,k-j} + \omega_{x,k} \tag{13}$$

(3) Time domain update of the estimation error covariance matrix:

$$P_{x,k+1}^{-} = \left(A_{x,k} - K_{x,1}\right) P_{x,k}^{+} \left(A_{x,k} - K_{x,1}\right)^T + Q_{x,k} + \sum_{j=2}^{k} K_{x,j} P_{x,k-j}^{+} K_{x,j}^{T} \tag{14}$$

(4) Calculating the Kalman gain matrix:

$$K_{x,k} = P_{x,k}^{-} C_{x,k}^{T} \left[C_{x,k} P_{x,k}^{-} C_{x,k}^{T} + R_{x,k}\right]^{-1} \tag{15}$$

(5) State estimate measurement update:

$$\widehat{x}_{x,k+1}^{+} = \widehat{x}_{x,k+1}^{-} + K_{x,k}\left(y_{k+1} - g\left(\widehat{x}_{x,k+1}^{+}, u_{k+1}\right)\right) \tag{16}$$

(6) Calculating the residual sequence:

$$\xi_{x,i} = \left(y_i - g\left(\widehat{x}_{x,i}^{+}, u_i\right)\right) \tag{17}$$

(7) Measurement update of the estimation error covariance matrix:

$$P_{x,k+1}^{+} = \left(I - K_{x,k} C_{x,k}\right) P_{x,k+1}^{-} \tag{18}$$

(8) Updating the adaptive noise:

$$\begin{cases} R_{x,k} = \dfrac{1}{M} \displaystyle\sum_{i=k-M+1}^{k} \xi_{x,i} {\xi_{x,i}}^{T} + C_{x,k} P_{x,k+1}^{+} C_{x,k}^{T} \\ Q_{x,k} = P_{x,k+1}^{+} - \left(A_{x,k} - K_{x,1}\right) P_{x,k}^{+} \left(A_{x,k} - K_{x,1}\right)^T + \displaystyle\sum_{j=2}^{k} K_{x,j} P_{x,k-j}^{+} K_{x,j}^{T} + \dfrac{1}{M} \displaystyle\sum_{i=k-M+1}^{k} \left(\widehat{x}_{x,i}^{+} - \widehat{x}_{x,i}^{-}\right)\left(\widehat{x}_{x,i}^{+} - \widehat{x}_{x,i}^{-}\right)^T \end{cases} \tag{19}$$

The $x_{x,k}$, $P_{x,k}$, $R_{x,k}$, $Q_{x,k}$ represent different estimated states, error covariance matrix, measurement noise error covariance matrix, and system noise error covariance matrix, respectively.

The flow chart of the DAFOEKF is shown in Fig. 2. The first filter AFOEKF$_1$ estimates the SOC state, $x_{1,k}$, and the second filter AFOEKF$_2$, synchronously estimates the SOE state, $x_{2,k}$. The two estimators exchange information recursively at each step to achieve closed-loop feedback. Furthermore, the selection of the same filter can effectively avoid cross-interference in the filtering process.

3.2. *A combined estimation method for SOE and SOC with maximum available energy prediction*

Based on the OCV correction value, the state space equation is established to predict the maximum available energy. OCV is a function of SOE and temperature, which will change slowly with the aging of the lithium battery. To further accurately obtain the OCV at each moment, it needs to be corrected according to the value of the previous moment, as shown in Eq. (20).

$$\begin{aligned} U_{OCV,k} &= U_{OCV,k-1} + \Delta_{OCV} \\ \Delta_{OCV} &= \frac{dU_{OCV}}{dt} = \frac{d(SOE,T)}{dSOE} \cdot \frac{dSOE}{dt} + \frac{d(SOE,T)}{dT} \cdot \frac{dT}{dt} \end{aligned} \tag{20}$$

A reliable thermal system can ensure that the internal temperature of the battery changes slowly, so the temperature change tends to zero. According to the definition of SOE, the expression of terminal voltage is shown in Eq. (21).

$$\begin{cases} \dfrac{dSOE}{dt} = \dfrac{\eta_{ED}(I) I U \Delta T}{\eta_e(I) E} \\ U_{OCV,k} = U_{OCV,k-1} + \dfrac{d(SOE,T)}{dSOE} \cdot \dfrac{dSOE}{dt} \end{cases} \tag{21}$$

where E represents the maximum available energy, and the change between two times is expressed by r. Combined with the fractional-order discrete state-space equation, *[E OCV UP_1 UP_2]* is selected as the state variable, and the fourth-order AEKF is adopted to predict the maximum available energy. The state-space equation is shown in Eq. (22).

$$\begin{cases} E_k = E_{k-1} + r \\ U_{OCV,k} = U_{OCV,k-1} + \dfrac{d(SOE,T)}{dSOE} \cdot \dfrac{\eta_{ED}(I) I_{k-1} U_{k-1} \Delta T}{\eta_e(I) E} \\ U_{1,k} = U_{1,k-1} exp\left(-\dfrac{\Delta T}{C_1 R_1}\right) + I_{k-1} R_1 \left[1 - exp\left(-\dfrac{\Delta T}{C_1 R_1}\right)\right] \\ U_{2,k} = U_{2,k-1} exp\left(-\dfrac{\Delta T}{C_2 R_2}\right) + I_{k-1} R_2 \left[1 - exp\left(-\dfrac{\Delta T}{C_2 R_2}\right)\right] \\ U_{L,k} = U_{OCV,k}(SOE) - U_{1,k} - U_{2,k} - I_k R_0 \end{cases} \tag{22}$$

The maximum available energy estimation based on AEKF can improve the stability of the system and reduce the cross-interference between the maximum available energy and SOE. The flow chart of the combined estimation method for SOE and SOC with maximum available energy prediction is shown in Fig. 3.

Based on the OCV correction value, the collaborative estimation between SOE and maximum available energy can eliminate the impact of using the fixed maximum available energy. The whole algorithm can not only improve the SOE accuracy under the terminal voltage and SOC constraints but also track the change of the maximum available energy, which improves the validity and SOE accuracy throughout the life cycle.

4. Experimental analysis

4.1. Experimental operating conditions

The whole experimental platform is composed of the battery test system, experimental battery, temperature control box, and host computer system, as shown in Fig. 4. The experimental lithium battery is placed in the temperature control box to ensure the stability of the experimental environment. The host computer system completes the step setting and automatically records the experimental data.

4.2. Experimental design of dynamic stress test

Considering the weather change factors, the following six typical dynamic stress test conditions are designed to simulate the working conditions of wireless sensor network nodes in terms of the discharge current, number of node users, intermittent power supply, and intermittent energy supply of lithium battery.

Fig. 5 (a) ~ (f) are the dynamic current curves under the operating conditions. Fig. 6 (a) ~ (f) are the voltage curves under the operating conditions. CS and CS1 working conditions correspond to continuous sunny (CS) days, with lithium batteries providing auxiliary energy. CR and CR1 working conditions correspond to continuous rainy (CR) days, with lithium batteries as the main energy source. SR and SR1 conditions correspond to the alternate sunny and rainy (SR) days. Two experimental conditions are designed under each weather condition according to the discharge current, number of node users, intermittent power supply, and intermittent power supply.

5. Results and verification

5.1. Horizontal comparison of operating condition experiment

Horizontal experiments are carried out to compare the calculation results of different SOE estimation algorithms under the CS conditions. The SOE estimation results are gradually analyzed from the aspects of the model parameter identification method, noise adaptive module, multi-constraint collaborative estimation, and maximum available energy prediction. The SOE comparison diagrams are obtained, as shown in Fig. 7.

The predicted SOE curve in Fig. 7 can well follow the reference curve, which shows the effectiveness of the algorithm for SOE estimation. The first line has noise interference, the SOE estimation results are gradually analyzed from the model parameter identification, multi-constraint collaborative estimation, and maximum available energy prediction. The experimental results clearly show that the prediction curve and reference curve of SOE is getting closer and closer, and the prediction error is getting smaller and smaller.

The second line is the SOE prediction curve after adding the noise adaptive filtering algorithm. Each vertical result is closer to the reference curve, and the error is gradually reduced. In Fig. 7 (a), the deviation between the estimated curve and the reference value is the largest because no influencing factors are corrected. Fig. 7 (h) has the best following effect and the smallest error due to the correction of the four influencing factors, and the estimation accuracy is better than the estimation result after correcting any other one, two, or three influencing factors, which proves the superiority and necessity of the algorithm.

Fig. 8 shows the accuracy and superiority of the algorithm more intuitively. In contrast, the curve in Fig. 8(h) is the smoothest, with the smallest error variation range, and is closest to the reference value, which verifies that the algorithm has the best prediction effect. Table 2 compares the errors of the eight algorithms from the RMSE and MAE, which shows that the proposed joint algorithm has the lowest RMSE (1.3 %) and MAE (1.14 %).

Horizontally, the error with a noise adaptive module in the same algorithm is much lower than that without a noise module, indicating the necessity of introducing the noise adaptive module. Vertically, the influence factors are revised cumulatively from top to bottom, exhibiting the improved SOE accuracy and reduced error with the increase of the modified influence factor.

Table 3 shows the percentage increase in RMSE and MAE for the stepwise stacking of the four influencing factors. Influence factor 1 corresponds to the change of parameter identification method, influence factor 2 is the application of the multi-constraint collaborative estimation algorithm, influence factor 3 is the real-time correction of the maximum available energy, and influence factor 4 is the superimposed noise adaptive module.

The results show that real-time tracking and correction of the four influencing factors is a necessary way to realize the construction of an SOE estimation model with high precision and strong adaptability, which can significantly improve the estimation accuracy and provide a strong guarantee for the prediction of the remaining available time of the lithium-ion battery.

5.2. Longitudinal comparison of operating condition experiment

5.2.1. Comparison of SOE results with fixed maximum available energy

Six representative operating conditions are selected for longitudinal experimental verification to further verify the accuracy and robustness of the algorithm. The SOE comparison diagrams under fixed maximum available energy are obtained, as shown in Fig. 9.

Fig. 9 shows that the SOE estimation results can follow the reference value in most conditions, but the error will increase at the end of the discharge, and even the results will diverge in some conditions. The reason is that the maximum available energy is a slowly changing quantity, which increases when the current changes sharply. If the fixed maximum available energy is still used, it will inevitably lead to differences in the estimation results.

The error comparison chart in Fig. 10 shows that the error of each operating condition can be controlled by 6 % except at the beginning and end of discharge. Due to the large discharge current and long discharge duration, the CR quickly reaches the cut-off voltage within the number of cycles, but the internal electric capacity is not fully discharged, resulting in a large error of the maximum available energy and divergence in the estimation results.

5.2.2. Comparison of SOE results with maximum available energy prediction

The predicted maximum available energy in the whole life cycle under different operating conditions is obtained through the fourth-order EKF algorithm, as shown in Fig. 11. The red line represents the fixed maximum available energy, and the green line represents the predicted maximum available energy. In addition to the initial convergence time required, the predicted maximum available energy has been fluctuating around a fixed value, and the energy value at each moment can be accurately predicted.

Fig. 12 proves that the change of the maximum available energy is very small, and the deviation range is controlled by 1 %. The deviation values of CR and CS1 are the largest, which are 0.86 % and 0.88 % respectively. The conclusions are consistent with the results in Fig. 9 (f) and Fig. 9 (d), which further show that the error of the maximum available energy will have a great impact on estimation accuracy.

Fig. 13 proves that the SOE estimation results obtained by the joint algorithm can well follow the reference value, even when the current changes drastically at the beginning and end of the discharge, the tracking effect of each operating condition is very good, without too much error deviation and result divergence. Whether the current changes frequently alternately or the discharge reaches the cut-off voltage in advance, the maximum available energy has been effectively corrected, which further improves the SOE accuracy and robustness.

Compared with Fig. 10, the error curve of Fig. 14 is smoother and the change is more gradual. The RMSE of each operating condition can be controlled by 2 %, and the error will not suddenly increase even at the discharge end with large current changes. Especially for the CR condition where the SOE estimation diverges in Fig. 9(f), the corrected error is about 0.5 %, and the accuracy is significantly improved.

Table 4 shows the error comparison between the fixed maximum available energy and the predicted maximum available energy under different operating conditions.

Table 4 shows that the RMSE of predicted maximum available energy under each operating condition is much smaller than that under fixed maximum available energy, indicating that it is quite necessary to up-date the maximum available energy in real-time and perform an adaptive correction of SOE, which can realize SOE estimation with high precision and strong robustness.

6. Conclusions

Since the maximum available energy will change with the ambient temperature and current, it is difficult to obtain an accurate SOE. A joint estimation algorithm of SOE and maximum available energy based on the FOC-ECM is proposed to improve the accuracy in the whole life cycle. The ADFOEKF is used to jointly estimate SOC and SOE to realize the state collaborative estimation under multiple constraints, and the fourth-order EKF is used to modify the maximum available energy in real-time to realize the joint estimation of maximum available energy and SOE. Since the maximum available energy will change with the ambient temperature and current, it is necessary to study the impact of temperature on the SOE estimation accuracy, which will also be our future research work. The original contribution of the article can be summarized as:

(1). The ADFOEKF algorithm is applied to the joint estimation of SOC and SOE to further eliminate the coupling between parameters and achieve multi-constraint state collaborative estimation.

(2). A fourth-order EKF algorithm is proposed for the collaborative estimation between SOE and maximum available energy, and the maximum available energy is corrected in real time to achieve SOE estimation with high accuracy and strong robustness, which can avoid the divergence of estimation results when using fixed maximum available energy.

(3). The experimental results are verified from different dimensions, and the horizontal comparison experiment compares four factors that affect SOE accuracy under CS conditions. The results show that real-time tracking and correction of the four influencing factors is a necessary way to realize the SOE estimation model with high precision and strong adaptability, which can significantly improve the estimation accuracy and provide a strong guarantee for the prediction of the remaining available time of the lithium-ion battery.

(4). Six typical dynamic stress test conditions of wireless sensor network nodes are selected to represent the load power supply of the node under different weather conditions, which are related to the node interactive users, discharge rate, intermittent supplementary power, and intermittent energy supply. The experimental results show that the error under each working condition is controlled within 2 %, which further verifies the adaptability and robustness of the algorithm, more consistent with the actual working conditions.

CRediT authorship contribution statement

Lei Chen: Conceptualization, Data curation, Methodology, Writing – original draft. **Shunli Wang:** Validation, Supervision. **Hong Jiang:** Software, Resources. **Carlos Fernandez:** Formal analysis, Writing – review & editing.

Declaration of competing interest

The authors declare that they have no known competing financial interests or personal relationships that could have appeared to influence the work reported in this paper.

Data availability

Data will be made available on request.

Acknowledgments

The work is supported by the National Natural Science Foundation of China (No. 61801407), Natural Science Foundation of Sichuan Province (No. 2023NSFSC1436), China Scholarship Council (No. 201908515099), and Fund of Robot Technology Used for Special Environment Key Laboratory of Sichuan Province (No. 18kftk03).

References

[1] M. Prauzek, et al., Energy harvesting sources, storage devices and system topologies for environmental wireless sensor networks: a review, Sensors (Basel) 18 (2018), https://doi.org/10.3390/s18082446.

[2] SJRSRJMDAKAS, Self-powered wireless sensor network framework to monitor bin level, J. Solid Waste Technol. Manag. 43 (2017).

[3] X. Hu, L. Xu, X. Lin, M. Pecht, Battery lifetime prognostics, Joule 4 (2020) 310–346, https://doi.org/10.1016/j.joule.2019.11.018.

[4] L. Zheng, L. Zhang, J. Zhu, G. Wang, J. Jiang, Co-estimation of state-of-charge, capacity and resistance for lithium-ion batteries based on a high-fidelity electrochemical model, Appl. Energy 180 (2016) 424–434, https://doi.org/ 10.1016/j.apenergy.2016.08.016.

[5] J.I. Hidalgo-Reyes, J.F. Gómez-Aguilar, R.F. Escobar-Jimenez, V.M. Alvarado- Martinez, M.G. Lopez-Lopez, Determination of supercapacitor parameters based on fractional differential equations, Int. J. Circ. Theory Appl. (2019), https://doi.org/ 10.1002/cta.2640.

[6] Y. Wang, M. Li, Z. Chen, Experimental study of fractional-order models for lithium- ion battery and ultra-capacitor: modeling, system identification, and validation, Appl. Energy 278 (2020), 115736, https://doi.org/10.1016/j.apenergy.2020.115736.

[7] C.I. Muresan, I.R. Birs, E.H. Dulf, D. Copot, L. Miclea, A review of recent advances in fractional-order sensing and filtering techniques, Sensors (Basel) 21 (2021), https://doi.org/10.3390/s21175920.

[8] J.I. Hidalgo-Reyes, J.F. Gomez-Aguilar, R.F. Escobar-Jimenez, V.M. Alvarado- Martinez, M.G. Lopez-Lopez, Classical and fractional-order modeling of equivalent electrical circuits for supercapacitors and batteries, energy management strategies for hybrid systems and methods for the state of charge estimation: a state of the art review, Microelectron. J. 85 (2019) 109–128, https://doi.org/10.1016/j.mejo.2019.02.006.

[9] M.M. Khader, J.F. Gómez-Aguilar, M. Adel, Numerical study for the fractional RL, RC, and RLC electrical circuits using legendre pseudo-spectral method, Int. J. Circ. Theory Appl. 49 (2021) 3266–3285, https://doi.org/10.1002/cta.3103.

[10] X. Tang, Y. Wang, K. Yao, Z. He, F. Gao, Model migration based battery power capability evaluation considering uncertainties of temperature and aging, J. Power Sources 440 (2019), 227141, https://doi.org/10.1016/j.jpowsour.2019.227141.

[11] X. Tang, et al., A novel framework for Lithium-ion battery modeling considering uncertainties of temperature and aging, Energy Convers. Manag. 180 (2019) 162–170, https://doi.org/10.1016/j.enconman.2018.10.082.

[12] Z. Wei, J. Zhao, D. Ji, K.J. Tseng, A multi-timescale estimator for battery state of charge and capacity dual estimation based on an online identified model, Appl. Energy 204 (2017) 1264–1274, https://doi.org/10.1016/j.apenergy.2017.02.016.

[13] C. Lin, H. Mu, R. Xiong, J. Cao, Multi-model probabilities based state fusion estimation method of lithium-ion battery for electric vehicles: state-of-energy, Appl. Energy 194 (2017) 560–568, https://doi.org/10.1016/j.apenergy.2016.05.065.

[14] X. Li, J. Xu, J. Hong, J. Tian, Y. Tian, State of energy estimation for a series- connected lithium-ion battery pack based on an adaptive weighted strategy, Energy 214 (2021), 118858, https://doi.org/10.1016/j.energy.2020.118858.

[15] R. Xiong, Q. Yu, L.Y. Wang, C. Lin, A novel method to obtain the open circuit voltage for the state of charge of lithium ion batteries in electric vehicles by using H infinity filter, Appl. Energy 207 (2017) 346–353, https://doi.org/10.1016/j. apenergy.2017.05.136.

[16] Y.Z. Zhang, H.W. He, R. Xiong, A data-driven based state of energy estimator of Lithium-ion batteries used to supply electric vehicles, Energy Procedia 75 (2015) 1944–1949, https://doi.org/10.1016/j.egypro.2015.07.228.

[17] Y. Wang, D. Yang, X. Zhang, Z. Chen, Probability based remaining capacity estimation using data-driven and neural network model, J. Power Sources 315 (2016) 199–208, https://doi.org/10.1016/j.jpowsour.2016.03.054.

[18] R. Xiong, J. Wang, W. Shen, J. Tian, H. Mu, Co-estimation of state of charge and capacity for lithium-ion batteries with multi-stage model fusion method, Engineering 7 (2021) 1469–1482, https://doi.org/10.1016/j.eng.2020.10.022.

[19] X. Zhang, Y. Wang, J. Wu, Z. Chen, A novel method for lithium-ion battery state of energy and state of power estimation based on multi-time-scale filter, Appl. Energy 216 (2018) 442–451, https://doi.org/10.1016/j.apenergy.2018.02.117.

[20] Z. Liu, et al., Fractional variable-order calculus based state of charge estimation of Li-ion battery using dual fractional order Kalman filter, J. Energy Storage 52 (2022), 104685, https://doi.org/10.1016/j.est.2022.104685.

[21] J. Chang, M. Chi, T. Shen, Model based state-of-energy estimation for LiFePO4 batteries using unscented particle filter, J. Power Electron. 20 (2020) 624–633, https://doi.org/10.1007/s43236-020-00051-5.

[22] P. Nian, Z. Shuzhi, Z. Xiongwen, Co-estimation for capacity and state of charge for lithium-ion batteries using improved adaptive extended Kalman filter, J. Energy Storage 40 (2021), 102559, https://doi.org/10.1016/j.est.2021.102559.

[23] Z. Shuzhi, G. Xu, Z. Xiongwen, A novel one-way transmitted co-estimation framework for capacity and state-of-charge of lithium-ion battery based on double adaptive extended Kalman filters, J.Energy Storage 33 (2021), 102093, https:// doi.org/10.1016/j.est.2020.102093.

[24] Z. Liu, S. Chen, H. Wu, H. Huang, Z. Zhao, A combined state of charge estimation method for lithium-ion batteries using cubature Kalman filter and least square with gradient correction, Adv. Theory Simul. 5 (2021) 2100331, https://doi.org/ 10.1002/adts.202100331.

[25] W. Xu, J. Xu, J. Lang, X. Yan, A multi-timescale estimator for lithium-ion battery state of charge and state of energy estimation using dual H infinity filter, IEEE Access 7 (2019) 181229–181241, https://doi.org/10.1109/access.2019.2959396.

[26] J. Wang, L. Zhang, J. Mao, J. Zhou, D. Xu, Fractional order equivalent circuit model and SOC estimation of supercapacitors for use in HESS, IEEE Access 7 (2019) 52565–52572, https://doi.org/10.1109/access.2019.2912221.

[27] P. Shrivastava, T. Kok Soon, M.Y.I. Bin Idris, S. Mekhilef, S.B.R.S. Adnan, Combined state of charge and state of energy estimation of lithium-ion battery using dual forgetting factor-based adaptive extended Kalman filter for electric vehicle applications, IEEE Trans. Veh. Technol. 70 (2021) 1200–1215, https://doi. org/10.1109/tvt.2021.3051655.

[28] L. Ma, C. Hu, F. Cheng, State of charge and state of energy estimation for lithium- ion batteries based on a long short-term memory neural network, J. Energy Storage 37 (2021), 102440, https://doi.org/10.1016/j.est.2021.102440.

[29] S. Zhang, X. Guo, X. Zhang, An improved adaptive unscented kalman filtering for state of charge online estimation of lithium-ion battery, J. Energy Storage 32 (2020), 101980, https://doi.org/10.1016/j.est.2020.101980.

[30] S. Zhang, X. Zhang, Joint estimation method for maximum available energy and state-of-energy of lithium-ion battery under various temperatures, J. Power Sources 506 (2021), 230132, https://doi.org/10.1016/j.jpowsour.2021.230132.

[31] S. Zhang, N. Peng, X. Zhang, A variable multi-time-scale based dual estimation framework for state-of-energy and maximum available energy of lithium-ion battery, Int. J. Energy Res. 46 (2021) 2876–2892, https://doi.org/10.1002/er.7350.

[32] S. Zhang, X. Zhang, A multi time-scale framework for state-of-charge and capacity estimation of lithium-ion battery under optimal operating temperature range, J. Energy Storage 35 (2021), 102325, https://doi.org/10.1016/j.est.2021.102325.

[33] Y. Zhang, R. Xiong, H. He, W. Shen, Lithium-ion battery pack state of charge and state of energy estimation algorithms using a hardware-in-the-loop validation, IEEE Trans. Power Electron. 32 (2017) 4421–4431, https://doi.org/10.1109/ tpel.2016.2603229.

[34] L. Xia, A novel prior noise correction - adaptive extended Kalman filtering method for the full parameter and state-of-energy co- estimation of the lithium-ion batteries, Int. J. Electrochem. Sci. (2021), 21077, https://doi.org/10.20964/ 2021.07.30.

[35] L. Chen, S. Wang, H. Jiang, C. Fernandez, X. Xiong, A novel combined estimation method of online full-parameter identification and adaptive unscented particle filter for Li-ion batteries SOC based on fractional-order modeling, Int. J. Energy Res. 45 (2021) 15481–15494, https://doi.org/10.1002/er.6817.

[36] L. Chen, A novel fractional - order extended Kalman filtering method for on-line joint state estimation and parameter identification of the high power Li-ion batteries, Int. J. Electrochem. Sci. (2021), 210537, https://doi.org/10.20964/ 2021.05.64.

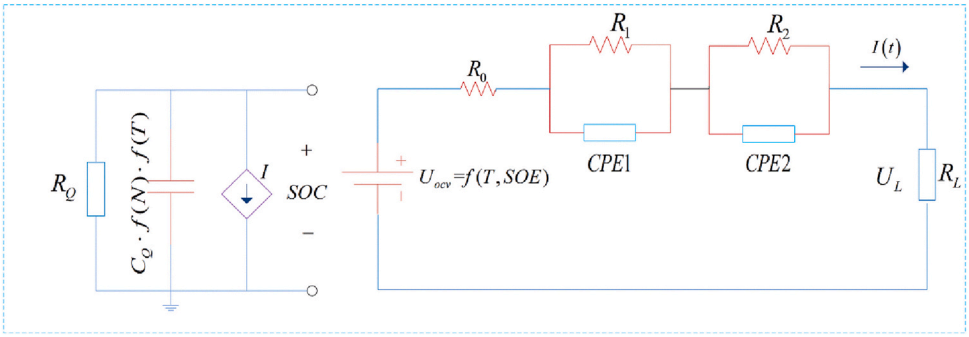

Fig. 1. The fractional-order composite equivalent circuit model.

Table 1
Model full-parameter identification process based on FFRLS.

(1) Parameter identification of OCV model	(2) Parameter identification of battery model
(a) Initialization	(a) Initialization
$\begin{cases} \varphi_{1,0} = [1 \quad -SOE_0 \quad -1/SOE_0 \quad lnSOE_0 \quad ln(1-SOE_0)\ ] \\ \theta_{1,0} = [(1-a_1-a_2)k_0 \quad (1-a_1-a_2)k_1 \quad (1-a_1-a_2)k_2 \quad (1-a_1-a_2)k_3 \quad (1-a_1-a_2)k_4\ ] \end{cases}$	$\begin{cases} \varphi_{2,0} = [y_2 \quad y_1 \quad i_0 \quad i_1 \quad i_2] \\ \theta_{2,0} = [a_1 \quad a_2 \quad a_3 \quad a_4 \quad a_5] \end{cases}$
(b) Calculate gain $K_{1,\ k}$ and error covariance matrix $P_{1,\ k}$	(b) Calculate gain $K_{2,\ k}$ and error covariance matrix $P_{2,\ k}$
$\begin{cases} K_{1,k} = P_{1,k-1}\varphi_{1,k}\left[\varphi_{1,k}^T P_{1,k-1}\varphi_{1,k} + \lambda_1\right]^{-1} \\ P_{1,k} = \lambda_1^{-1}\left[I - K_{1,k}\varphi_{1,k}^T\right]P_{1,k-1} \end{cases}$	$\begin{cases} K_{2,k} = P_{2,k-1}\varphi_{2,k}\left[\varphi_{2,k}^T P_{2,k-1}\varphi_{2,k} + \lambda_2\right]^{-1} \\ P_{2,k} = \lambda_2^{-1}\left[I - K_{2,k}\varphi_{2,k}^T\right]P_{2,k-1} \end{cases}$
(c) Calculate the error $e_{1,\ k}$ and update model parameter $\widehat{\theta}_{1,k}$	(c) Calculate the error $e_{2,\ k}$ and update model parameter $\widehat{\theta}_{2,k}$
$\begin{cases} e_{1,k} = y_{1,k} - \varphi_{1,k}^T\widehat{\theta}_{1,k-1} \\ \widehat{\theta}_{1,k} = \widehat{\theta}_{1,k-1} + K_{1,k}e_{1,k} \end{cases}$	$\begin{cases} e_{2,k} = y_{2,k} - \varphi_{2,k}^T\widehat{\theta}_{2,k-1} \\ \widehat{\theta}_{2,k} = \widehat{\theta}_{2,k-1} + K_{2,k}e_{2,k} \end{cases}$
(d) Update the predicted $U_{oc,\ k}$	(d) Update the predicted $U_{L,\ k}$
$U_{ocv,k} = \varphi_{1,k}\widehat{\theta}_{1,k}$	$U_{L,k} = \varphi_{2,k}\widehat{\theta}_{2,k}$

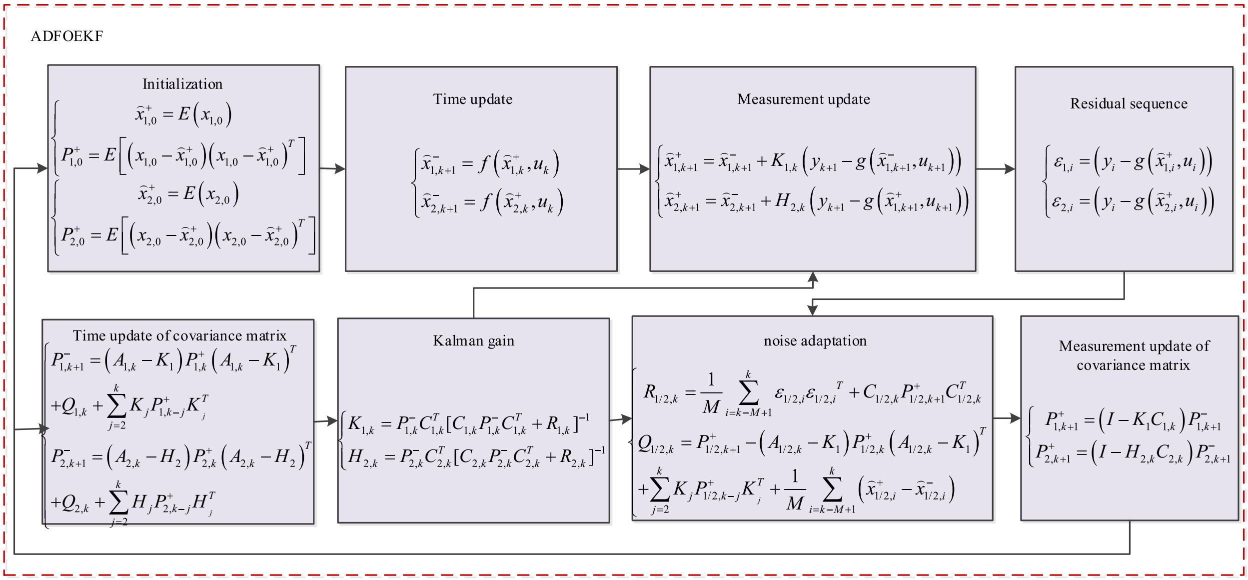

Fig. 2. The flow chart of the DAFOEKF algorithm.

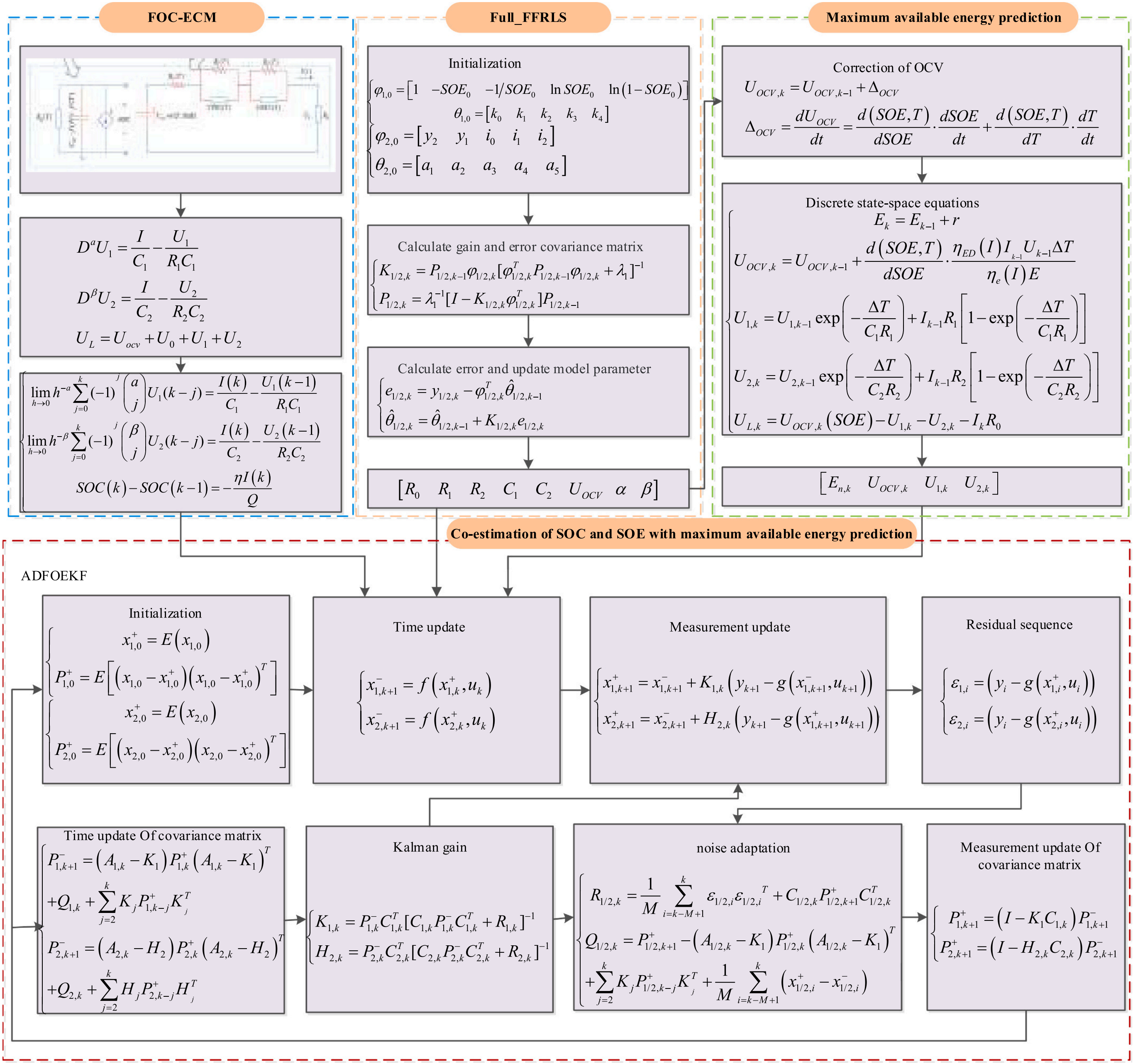

Fig. 3. The flow chart of the combined estimation method for SOE and SOC with maximum available energy prediction.

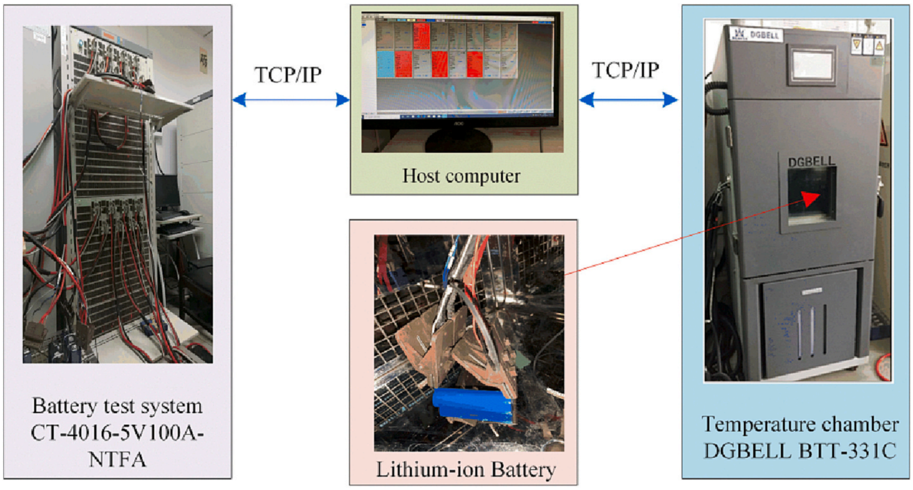

Fig. 4. The battery test bench.

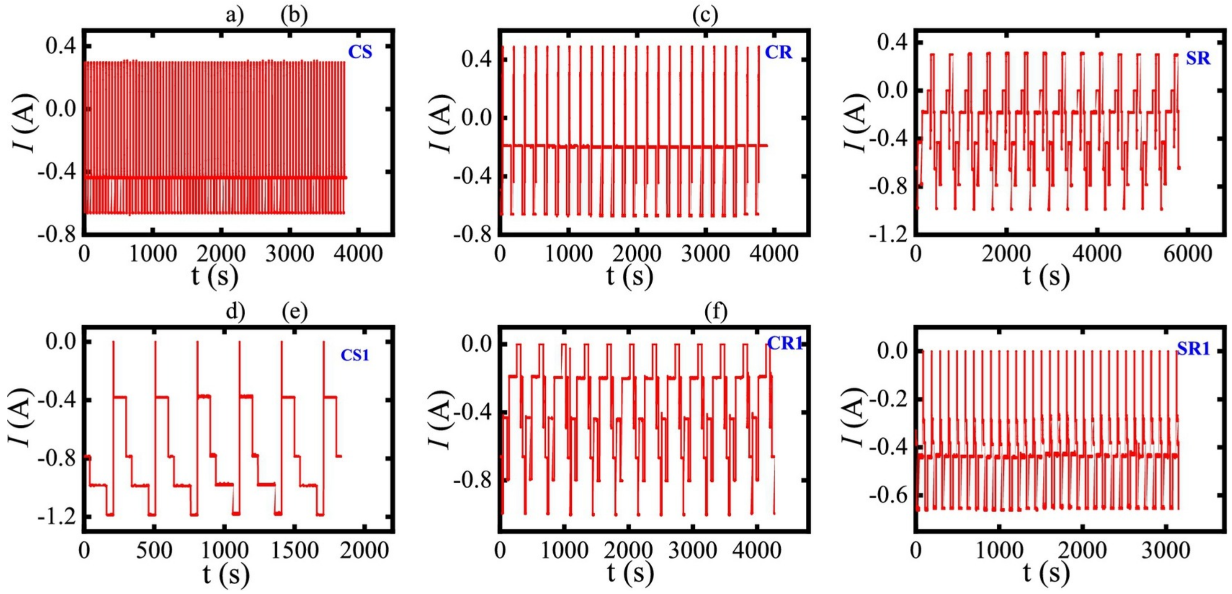

Fig. 5. (a) Dynamic current profile under CS operating conditions. (b) Dynamic current profile under CR operating conditions. (c) Dynamic current profile under SR operating conditions. (d) Dynamic current profile under CS1 operating conditions. (e) Dynamic current profile under CR1 operating conditions. (f) Dynamic current profile under SR1 operating conditions.

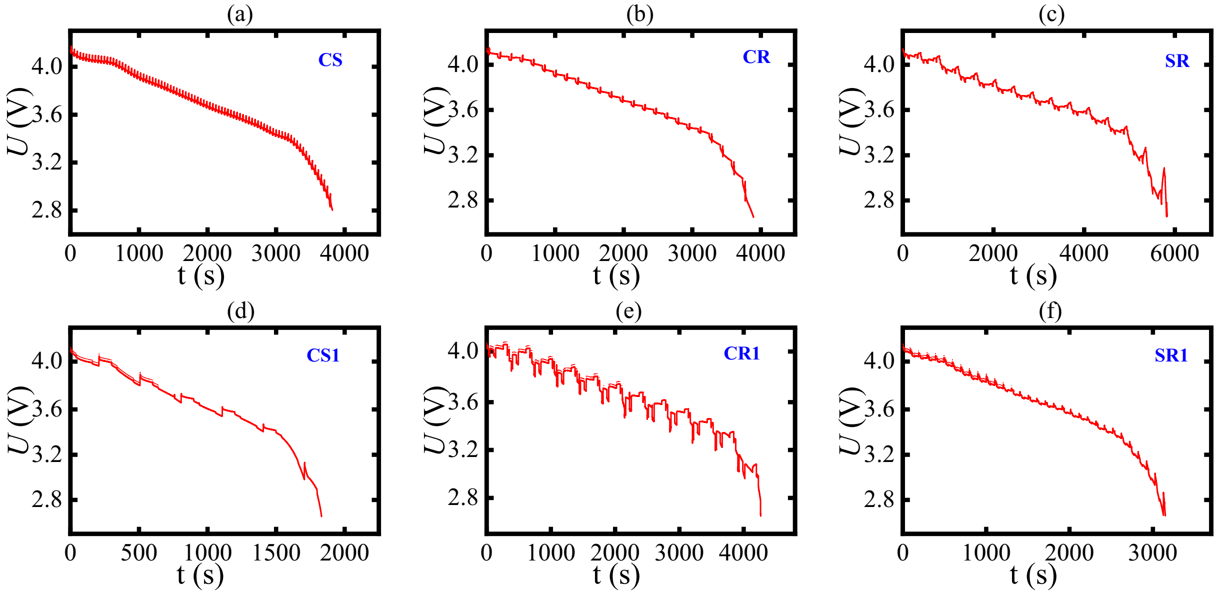

Fig. 6. (a) Voltage profile under CS operating conditions. (b) Voltage profile under CR operating conditions. (c) Voltage profile under SR operating conditions. (d) Voltage profile under CS1 operating conditions. (e) Voltage profile under CR1 operating conditions. (f) Voltage profile under SR1 operating conditions.

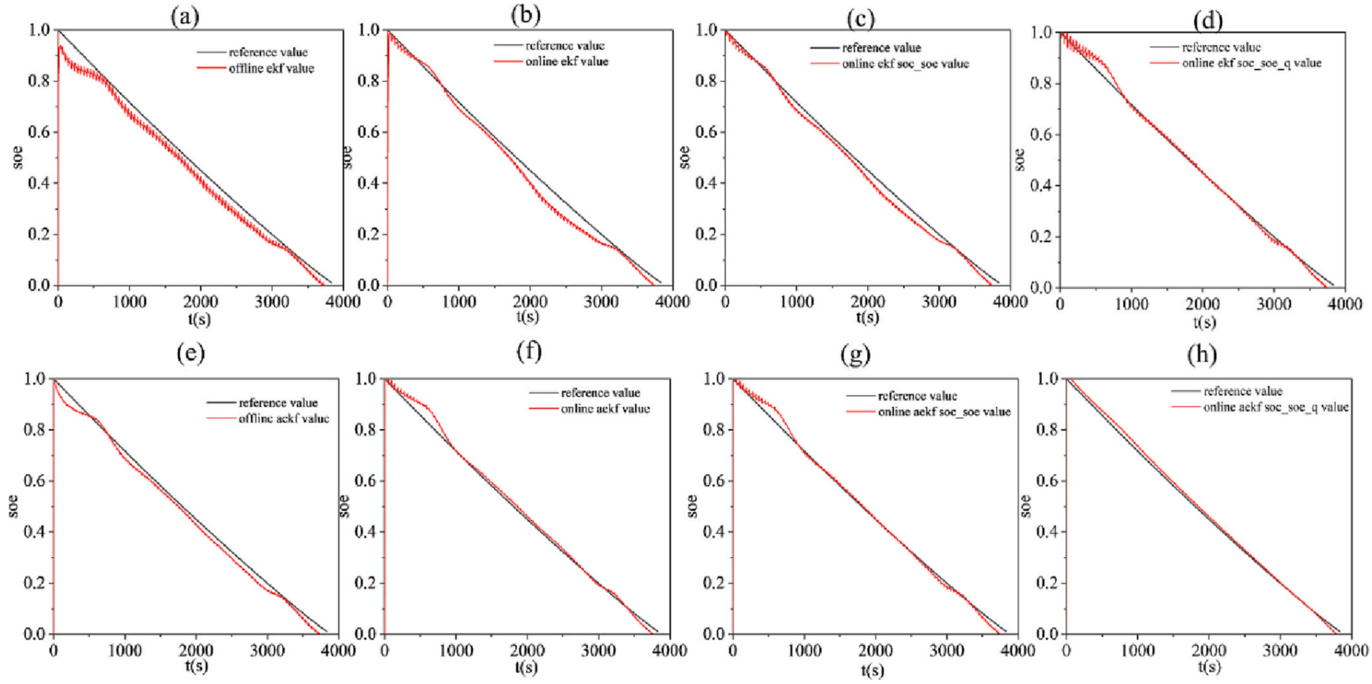

Fig. 7. (a) SOE estimation results under offline-EKF. (b) SOE estimation results under online-EKF. (c) Joint estimation results for SOC and SOE under online-EKF. (d) Joint estimation results for maximum available energy and SOE under online-EKF. (e) SOE estimation results under offline-AEKF. (f) SOE estimation results under online-AEKF. (g) Joint estimation results for SOC and SOE under online-AEKF. (h) Joint estimation results for maximum available energy and SOE under online-AEKF.

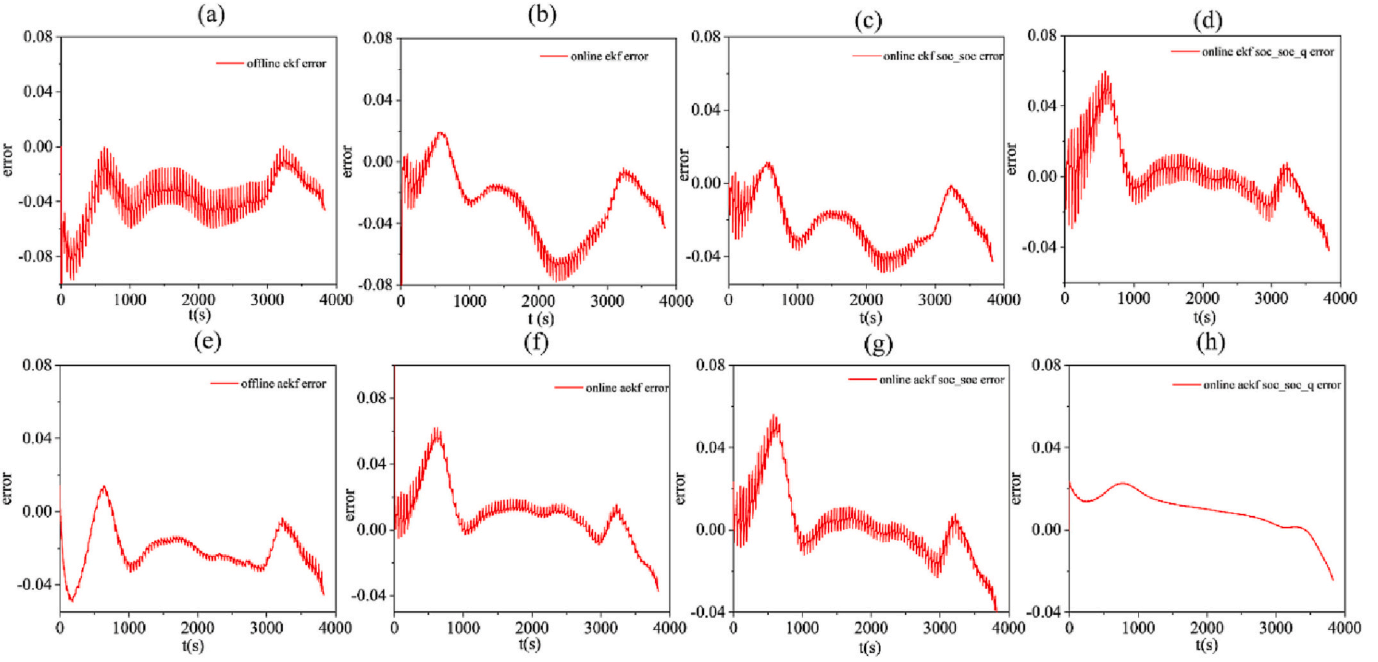

Fig. 8. (a) SOE error under offline-EKF. (b) SOE error under online-EKF. (c) Joint SOE error for SOC and SOE under online-EKF. (d) Joint SOE error for maximum available energy and SOE under online-EKF. (e) SOE error under offline-AEKF. (f) SOE error under online-AEKF. (g) Joint SOE error for SOC and SOE under online-AEKF. (h) Joint SOE error for maximum available energy and SOE under online-AEKF.

Table 2
The error comparison under different SOE algorithms.

SOE algorithms	Rmse	Mae	SOE algorithms	Rmse	Mae
Offline_ekf_soe	0.0458	0.0384	Offline_aekf_soe	0.0241	0.022
Online_ekf_soe	0.0406	0.0297	Online_aekf_soe	0.0198	0.0146
Online_ekf_soc_soe	0.0251	0.0221	Online_aekf_soc_soe	0.0173	0.0117
Online_ekf_soc_soe_q	0.0176	0.012	Online_aekf_soc_soe_q	0.013	0.0114

Table 3
The influence of four factors on SOE accuracy.

Influencing factors of SOE algorithm	Rmse improvement	Mae improvement
Influence factor 1	11.34 %	22.65 %
Influence factor 1+ Influence factor 2	38.18 %	25.59 %
Influence factor 1+ Influence factor 2+Influence factor 3	29.88 %	45.7 %
Influence factor 1+ Influence factor 2+ Influence factor 3+ Influence factor 4	26.1 %	5 %

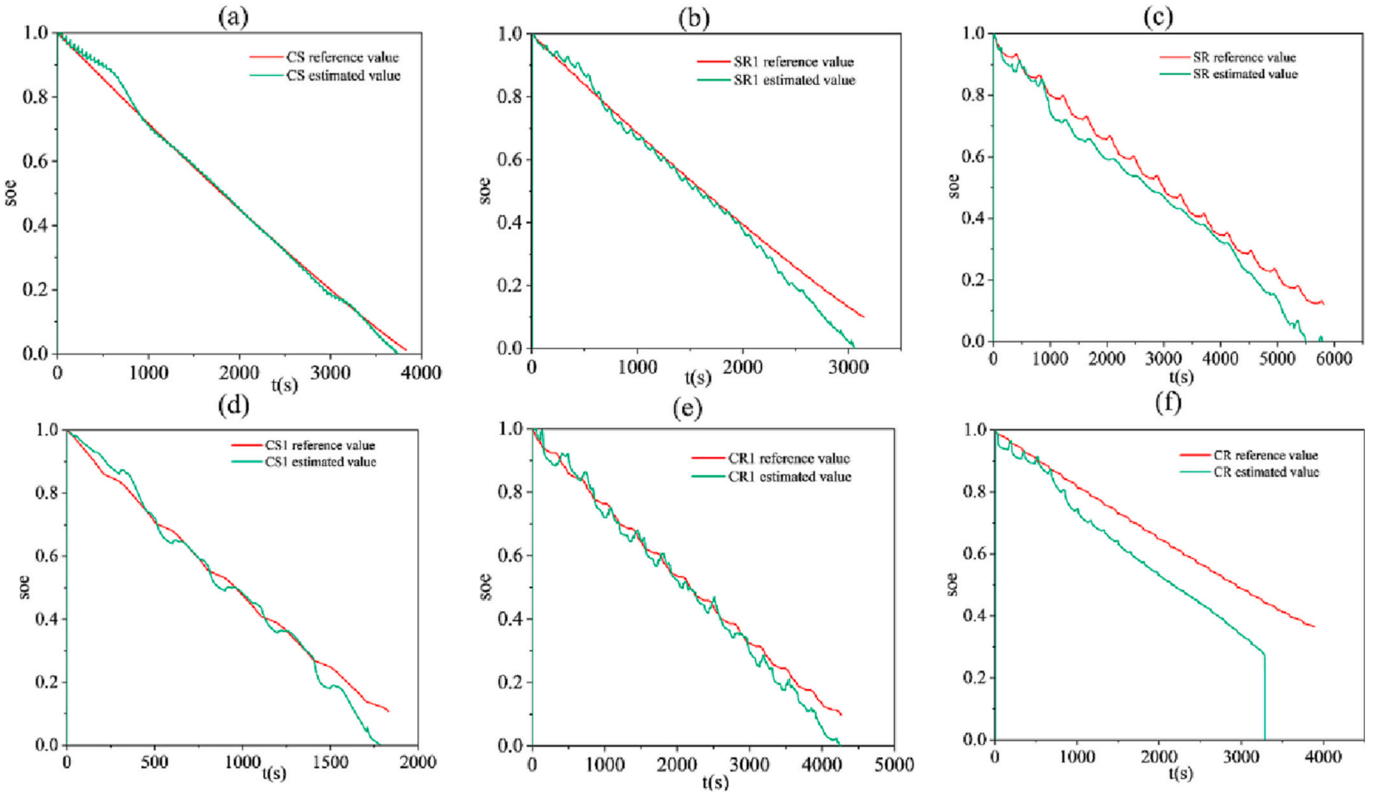

Fig. 9. (a) SOE estimation results under CS operating conditions. (b) SOE estimation results under SR1 operating conditions. (c) SOE estimation results under SR operating conditions. (d) SOE estimation results under CS1 operating conditions. (e) SOE estimation results under CR1 operating conditions. (f) SOE estimation results under CR operating conditions.

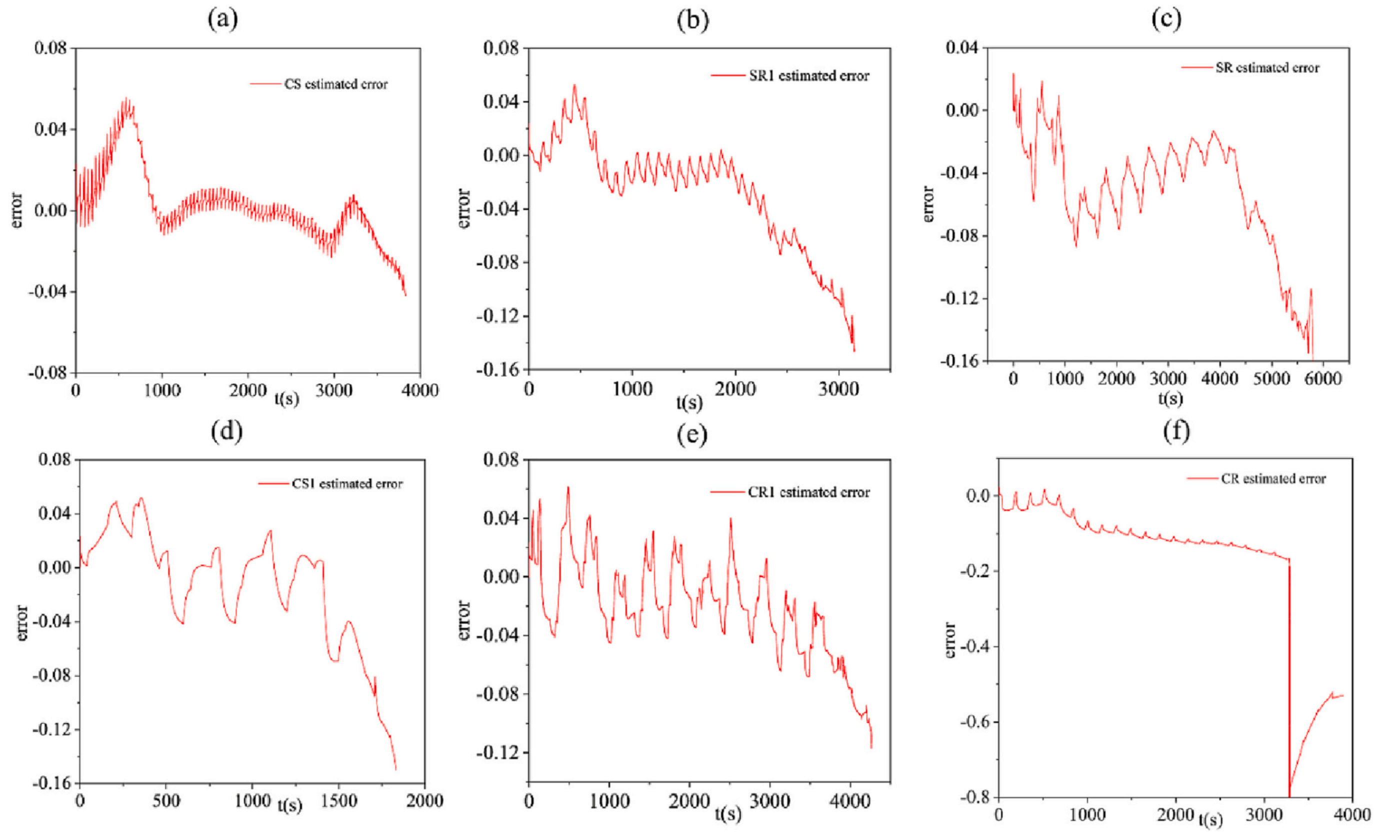

Fig. 10. (a) SOE error under CS operating conditions. (b) SOE error under SR1 operating conditions. (c) SOE error under SR operating conditions. (d) SOE error under CS1 operating conditions. (e) SOE error under CR1 operating conditions. (f) SOE error under CR operating conditions.

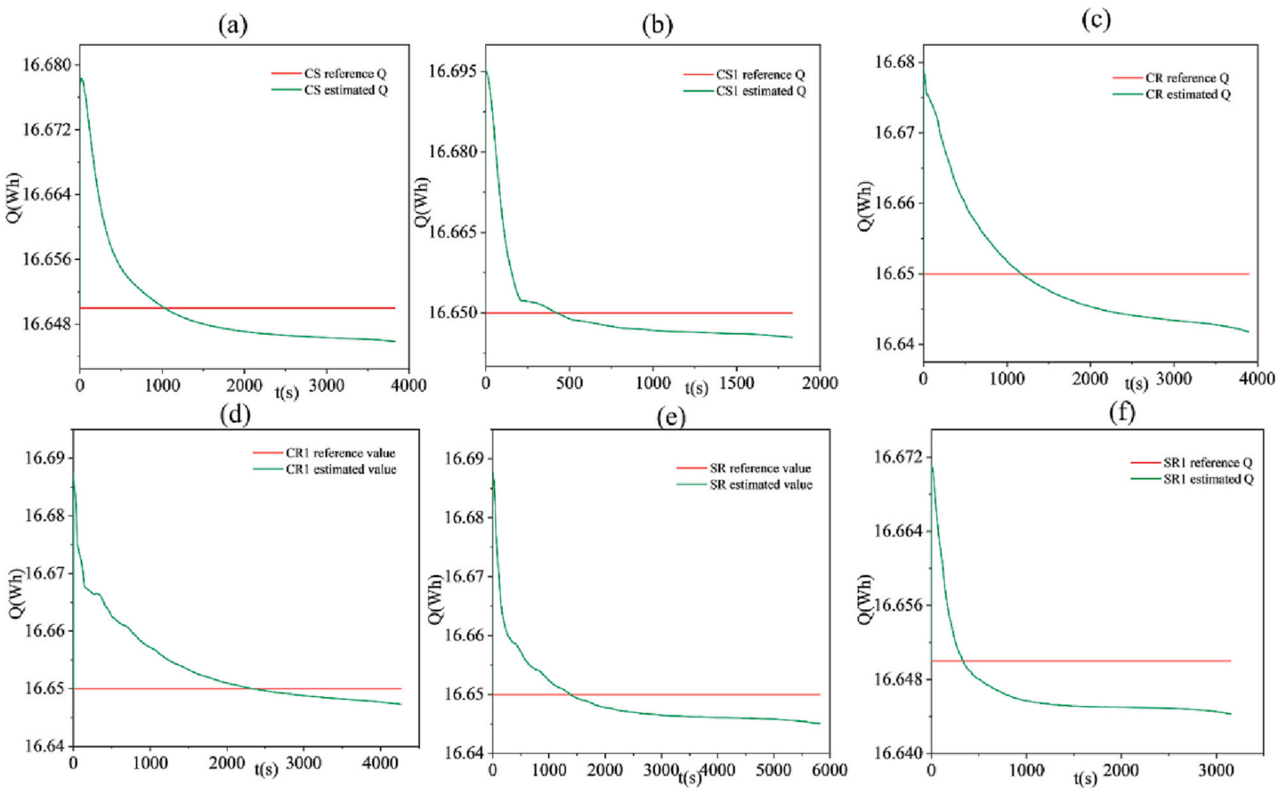

Fig. 11. (a) Predicted maximum available energy under CS operating conditions. (b) Predicted maximum available energy under CS1 operating conditions. (c) Predicted maximum available energy under CR operating conditions. (d) Predicted maximum available energy under CR1 operating conditions. (e) Predicted maximum available energy under SR operating conditions. (f) Predicted maximum available energy under SR1 operating conditions.

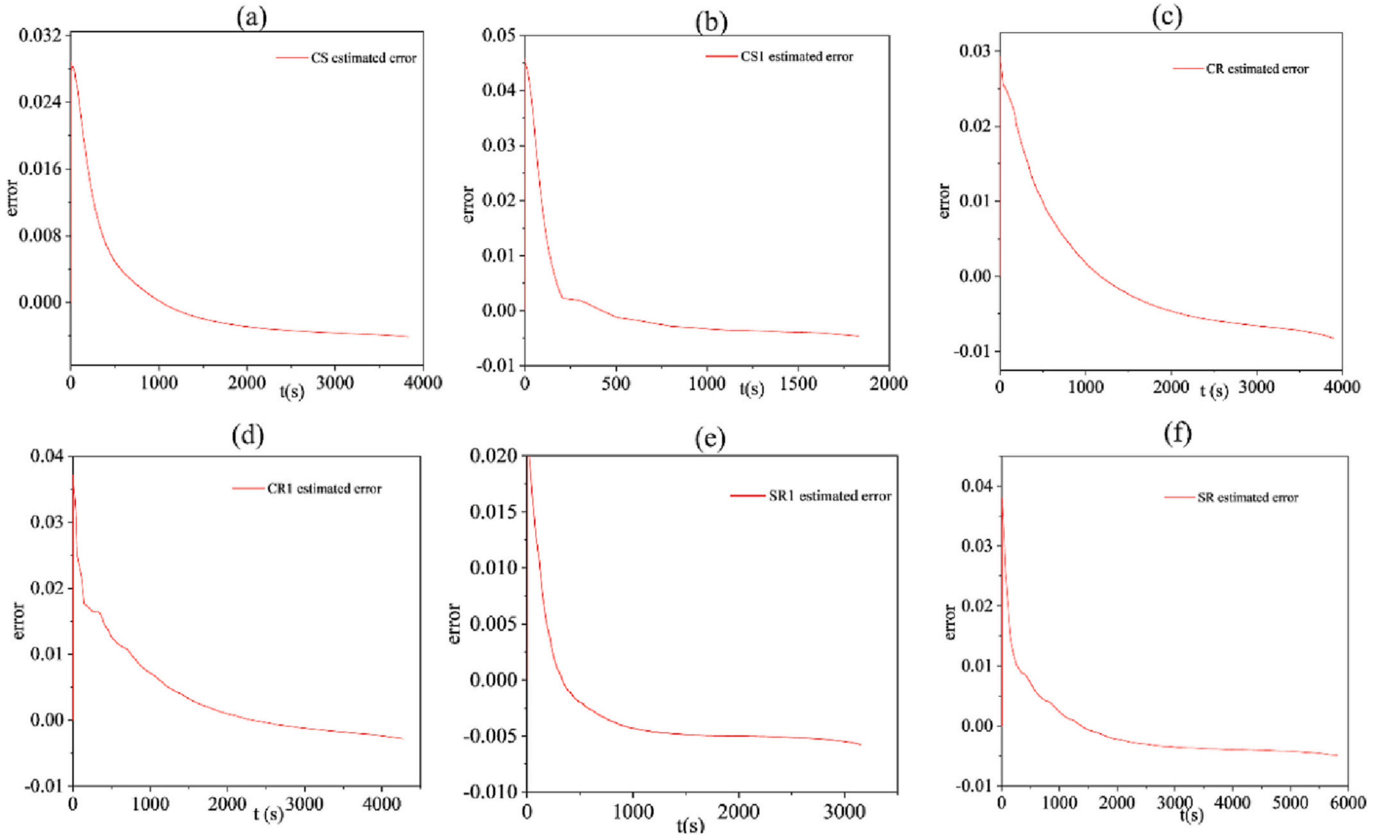

Fig. 12. (a) Predicted error under CS operating conditions. (b) Predicted error under CS1 operating conditions. (c) Predicted error under CR operating conditions. (d) Predicted error under CR1 operating conditions. (e) Predicted error under SR1 operating conditions. (f) Predicted error under SR operating conditions.

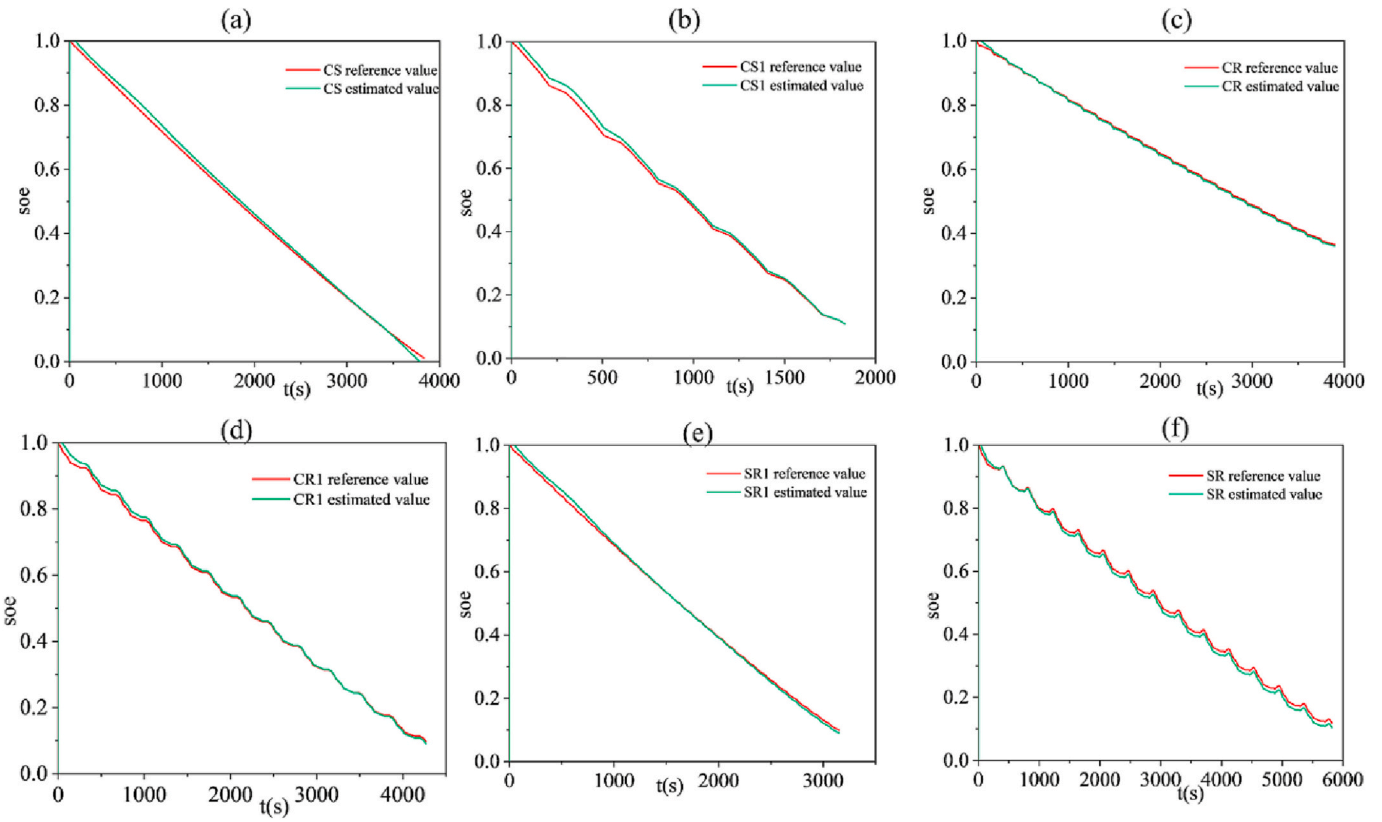

Fig. 13. (a) Predicted SOE estimation results under CS with maximum available energy. (b) Predicted SOE estimation results under CS1 with maximum available energy. (c) Predicted SOE estimation results under CR with maximum available energy. (d) Predicted SOE estimation results under CR1 with maximum available energy. (e) Predicted SOE estimation results under SR1 with maximum available energy. (f) Predicted SOE estimation results under SR with maximum available energy.

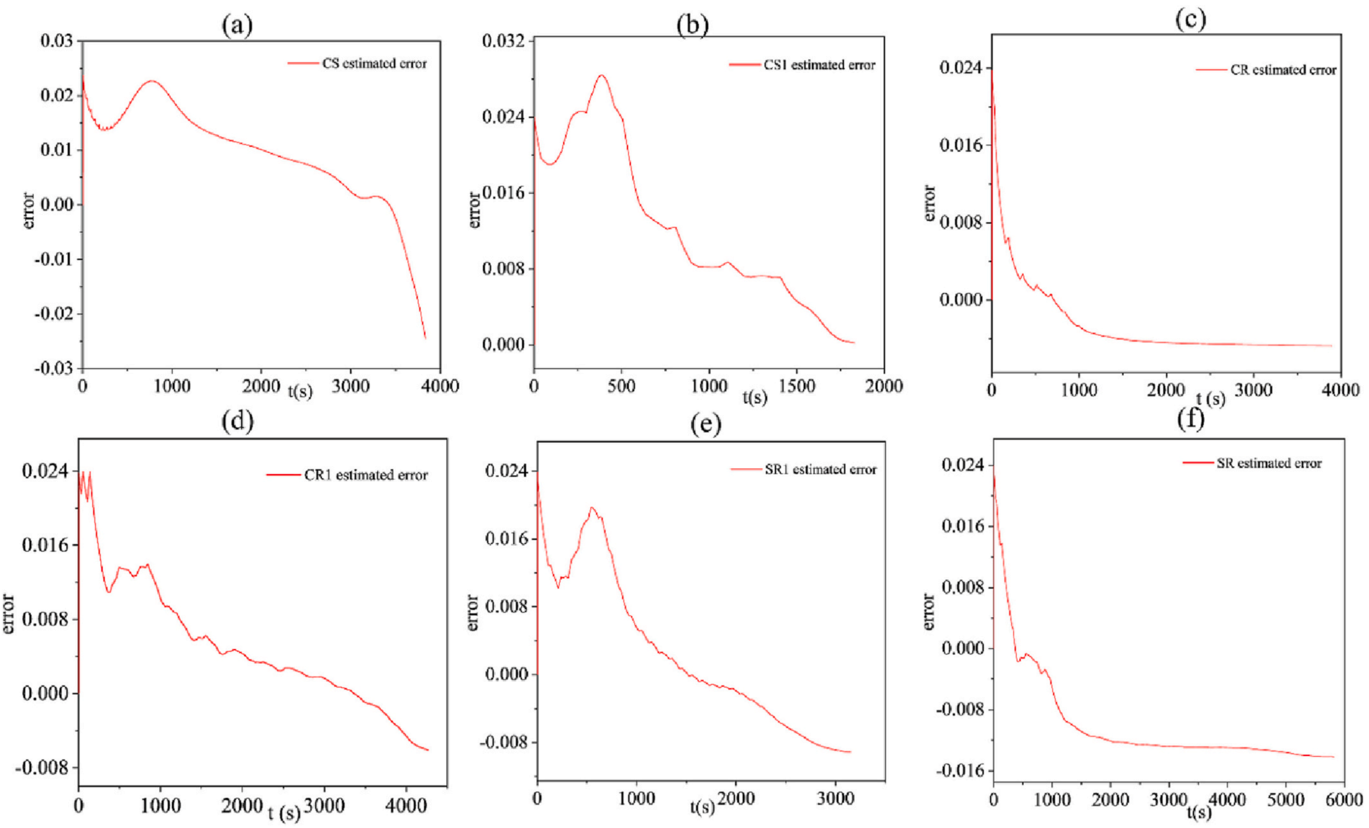

Fig. 14. (a) Predicted error results under CS with maximum available energy. (b) Predicted error results under CS1 with maximum available energy. (c) Predicted error results under CR with maximum available energy predicted. (d) Predicted error results under CR1 with maximum available energy. (e) Predicted error results under SR1 with maximum available energy. (f) Predicted error results under SR with maximum available energy.

Table 4
The comparison results of the maximum available energy for SOE estimation accuracy.

Error	Predicted maximum available energy			Fixed maximum available energy		
Conditions	Rmse	Mae	Mape	Rmse	Mae	Mape
CS	0.0130	0.0114	0.2745	0.0173	0.0117	0.2812
CS1	0.0148	0.0123	0.2983	0.0455	0.0324	0.785
CR	0.0049	0.0042	0.1012	0.2596	0.1746	4.2082
CR1	0.0083	0.0063	0.1545	0.0387	0.0307	0.7526
SR	0.0119	0.0113	0.2716	0.063	0.052	1.2548
SR1	0.0092	0.0073	0.1748	0.049	0.035	0.8406